中國機械工程學刊第四十一卷第四期第 467~478 頁(民國一百零九年)
Journal of the Chinese Society of Mechanical Engineers, Vol.41, No.4, pp 467~478 (2020)

A Tension Instability Free Smoothed Particle Hydrodynamics (SPH) Method Applied to Elastic Solid Mechanics

Xiaoying Zhang[a1], Zhe Hu[a2], Weicheng Cui [abc3]and Fang Wang[b4]

Keywords： smoothed particle hydrodynamics (SPH), elastic solid, tension instability, von Neumann stability analysis

ABSTRACT

In this paper, a simple algorithm applied to elastic solid problems based on the Smoothed Particle Hydrodynamics (SPH) method is discussed. The solid is considered to be not flowable, and therefore particle approximation is only performed on the initial undeformed solid domain using a typical Lagrange interpretation. Under such consideration, the algorithm shows palpable reduction in computational consumption, and suffers less from tension instability which happens in most traditional SPH methods for solids. The proposed algorithm is validated against theoretical solutions, and is tested in solving a contact and collision problem. A von Neumann stability analysis is performed and a sufficient condition of stability is given, showing that the tension instability issue can be avoided under certain circumstances.

INTRODUCTION

Grid or mesh based numerical methods such as the finite difference method (FDM) and the finite element method (FEM) play a crucial role in computational solid mechanics. One notable feature of grid based models is the division of a continuum domain into discrete small subdomains, which can be termed as discretization or meshing. Despite the great success in dealing with common structure problems, the mesh based methods meet challenge from aspects such as large deformation and crack evolution which may lead to grid distortion and solution failure. Over the past years, meshfree methods have raised wide attention and made great progress in both computational solid and fluid mechanics.

Being a meshfree method, smoothed particle hydrodynamics (SPH) was first intended to solve astrophysical problems in three-dimensional open space. Later it was extended to computational fluid mechanics, and then computational solid mechanics. In computational fluid mechanics, SPH was used to solve problems, such as compressible and incompressible flows (Monaghan, 1994; Zhang et al., 2017), viscous flows (Bouscasse et al., 2017; Xu and Deng, 2016), viscous flows with turbulence models (Hu and Adams, 2015; Ren et al., 2016) and free surface flows (Sarfaraz and Pak, 2017; Peng et al., 2017). In computational solid mechanics, SPH shows capacity of solving problems involving thin and thick shell structures (Lin et al., 2014), elastic solids (Sugiura and Inutsuka, 2017), and visco-plastic structures (Chikazawa et al., 2001). Since SPH was applicable to both solid and fluid issues, it was also used to solve fluid-structure interaction (FSI) problems (Antoci et al., 2007; Chikazawa et al., 2001). With the rapid development of CPU and GPU acceleration techniques, SPH has found its place in industrial usage and some open-source and commercial SPH solvers have been developed (Gómez-Gesteira et al., 2012). Maybe SPH will soon become a mature numerical technique just like finite volume method (FVM) and FEM.

However, when applied to solid dynamics, one problem known as tension instability arises. A common manifestation of tension instability is that the solution becomes unstable when part of the solid bears tensile stress. Usually special treatment should be carried out to overcome the tension instability problem. For instance, Dyka and Ingel (1995) proposed an approach to avoid tensile instability, in which stress was evaluated at points away from the SPH particles. With specially selected SPH equations for the calculation of strain and momentum, the tension instability was removed. Chen et al. (1999)

Paper Received October, 2018. Revised March, 2019, Accepted March, 2019, Author for Correspondence: Weicheng Cui.
a School of Marine Engineering, Jimei University, Xiamen, 361021, China.
b Shanghai Engineering Research Center of Hadal Science and Technology, Shanghai Ocean University, Shanghai 201306, China.
c School of Engineering, Westlake University, Hangzhou 310024, China.
1 PhD candidate.
2 Associate Professor.
3 Professor.
4.Associate researcher.

proposed a corrective Smoothed-Particle Method (CSPM) to address the tensile instability problem, in which a group of simultaneous particle equations was derived through Taylor series expansion. Yet additional computational efforts are required to solve these equations explicitly or numerically. Monaghan (2000) showed that tensile instability can be removed by using an artificial stress or an artificial pressure in case of fluids. Using this method, whether or not the material is in tension or compression should be better predetermined (Gray et al., 2001). Gray et al. (2001) improved Monaghan's method by basing the artificial stress on the sign of the principal stress. Sigalotti and Lopez (2008) proposed an adaptive density kernel estimation (ADKE) algorithm to remove tensile instability, in which the width of the kernel interpolant is allowed to vary locally in such a way that only the minimum necessary smoothing is applied to the data.

In this paper, a simple SPH approach solving elastic solid problems is adopted. In comparison against above-mentioned techniques of tension instability removal, this method is simple and requires no additional computational cost. The approach solves fundamental governing equations of elastic mechanics. Particle approximation is performed according to the initial state of the solid. The resulted approach reduces the number of partial derivative equations (PDEs) to be solved and shows good tolerance against tension instability. By conducting a 2-D von Neumann stability analysis, it is shown that tension instability is completely removed under certain condition. Validation is conducted by comparing the proposed approach against theoretical results. Finally, the approach is tested with a solid dynamic issue involving contact and collision events.

GOVERNING EQUATIONS

The mass conservation equation of continuum is

$$\frac{d\rho}{dt}+\rho\frac{\partial \boldsymbol{v}^{\beta}}{\partial \boldsymbol{x}^{\beta}}=0, \tag{1}$$

where ρ is density, $\boldsymbol{v}$ is velocity vector. We adopt summation convention for repeated indices of Greek letters. The α -th momentum equation of continuum is

$$\frac{d\boldsymbol{v}^{\alpha}}{dt}=\frac{1}{\rho}\frac{\partial \boldsymbol{\sigma}^{\alpha\beta}}{\partial \boldsymbol{x}^{\beta}}+\boldsymbol{f}^{\alpha}, \tag{2}$$

where $\boldsymbol{\sigma}$ is stress tensor and $\boldsymbol{f}$ is body force vector. The constitutive equation of isotropic elastic solid is written as follows

$$\boldsymbol{\sigma}^{\alpha\beta}=p\boldsymbol{\delta}^{\alpha\beta}+G\boldsymbol{\varepsilon}^{\alpha\beta}, \tag{3}$$

where $\boldsymbol{\delta}^{\alpha\beta}$ is the Kronecker delta, $\boldsymbol{\varepsilon}^{\alpha\beta}$ is strain tensor, $\boldsymbol{\sigma}^{\alpha\beta}$ is stress tensor. Shear modulus G equals $\frac{E}{1+\mu}$, where E is Young's modulus and μ is Poisson ratio. Pressure p equals $\frac{\mu G}{1-2\mu}\boldsymbol{\varepsilon}^{\alpha\alpha}$.

The geometry equations are

$$\boldsymbol{\varepsilon}^{\alpha\beta}=\frac{1}{2}\left(\frac{\partial \boldsymbol{s}^{\beta}}{\partial \boldsymbol{x}^{\alpha}}+\frac{\partial \boldsymbol{s}^{\alpha}}{\partial \boldsymbol{x}^{\beta}}\right), \tag{4}$$

$$\boldsymbol{v}^{\alpha}=\frac{d\boldsymbol{s}^{\alpha}}{dt}, \tag{5}$$

where $\boldsymbol{s}$ is displacement vector. By substituting Eq. (4)-(5) into Eq. (1) and assuming no residual stress exists at the initial moment, we have

$$\rho=\rho_0\cdot\exp\left(-\frac{1-2\mu}{\mu G}p\right), \tag{6}$$

where ρ_0 is density at initial moment. Eq. (6) gives the relationship between pressure and density, and therefore can be treated as some kind of state equation.

LAGRANGIAN SPH FORMULATION FOR SOLIDS

Basic SPH Equations

The particle-approximated momentum equation and constitutive equation are written as

$$\begin{aligned}\frac{d\boldsymbol{v}_i^{\alpha}}{dt}&=\sum_{j=1}^{N}m_j\left(\frac{p_i}{\rho_i^2}+\frac{p_j}{\rho_j^2}\right)\frac{\partial W_{ij}}{\partial \boldsymbol{x}_i^{\alpha}}\\&+\sum_{j=1}^{N}m_j\left(\frac{G_i\boldsymbol{\varepsilon}_i^{\alpha\beta}}{\rho_i^2}+\frac{G_j\boldsymbol{\varepsilon}_j^{\alpha\beta}}{\rho_j^2}\right)\frac{\partial W_{ij}}{\partial \boldsymbol{x}_i^{\beta}}+\boldsymbol{f}_i^{\alpha},\end{aligned} \tag{7}$$

$$p_i=\frac{\mu}{1-2\mu}G\boldsymbol{\varepsilon}_i^{\alpha\alpha}, \tag{8}$$

where subscripts i and j represent the i-th and j-th particles, W is the kernel function and $W_{ij}=W\left(\left|\boldsymbol{x}_i^{\alpha}-\boldsymbol{x}_j^{\alpha}\right|\right)$. The particle-approximated geometry equation is

$$\boldsymbol{\varepsilon}_i^{\alpha\beta}=\frac{1}{2}\sum_{j=1}^{N}\frac{m_j}{\rho_j}\boldsymbol{s}_{ji}^{\beta}\cdot\frac{\partial W_{ij}}{\partial \boldsymbol{x}_i^{\alpha}}+\frac{1}{2}\sum_{j=1}^{N}\frac{m_j}{\rho_j}\boldsymbol{s}_{ji}^{\alpha}\cdot\frac{\partial W_{ij}}{\partial \boldsymbol{x}_i^{\beta}}, \tag{9}$$

where $\boldsymbol{s}_{ji}^{\alpha}=\boldsymbol{s}_j^{\alpha}-\boldsymbol{s}_i^{\alpha}$.

A leap-frog algorithm is utilized for time discretization. Assuming Eq. (7)-(9) are carried out at time step n, the time advancing scheme is

$$\left(\boldsymbol{v}_i^{\alpha}\right)^{n+1/2}=\left(\boldsymbol{v}_i^{\alpha}\right)^{n-1/2}+\left(d\boldsymbol{v}_i^{\alpha}/dt\right)^{n}\Delta t, \tag{10}$$

$$\left(\boldsymbol{s}_i^{\alpha}\right)^{n+1}=\left(\boldsymbol{s}_i^{\alpha}\right)^{n}+\left(\boldsymbol{v}_i^{\alpha}\right)^{n+1/2}\Delta t, \tag{11}$$

where superscript n denotes function at the n-th time step, and Δt is the time difference between two adjacent time steps. At domain boundaries, Eq. (7) and Eq. (9) will lose precision due to the fact that only part of the integral region can be account for. To decline the boundary accuracy loss, the integral is normalized with a factor $\sum_{j=1}^{N}\frac{m_j}{\rho_j}W_{ij}$. Later in section 5, we give comparison on results obtained with and without normalization. It is noted that the algorithm of this paper should be limited to small-deformation issues with little rigid-body rotations.

Loads and Boundary Conditions

We apply constraints directly upon boundary particles. In dealing with contact and collision problems, a repulsive force is introduced to prevent different elastic solids (or rigid bodies) from penetrating into each other. The Lennard-Jones penalty force (Liu and Liu, 2010) is applied pairwisely on the two approaching particles along their centerline.

$$\boldsymbol{f}_{ij} = \begin{cases} \overline{p}\left(l^{n_1} - l^{n_2}\right)\dfrac{\boldsymbol{x}_{ij}}{r_{ij}^2}, & l \ge 1 \\ 0, & l < 1 \end{cases}, \quad l = \frac{kh_i + kh_j}{r_{ij}}, \tag{12}$$

where r_{ij} is the distance between particle i and j, kh_i is the non-zero "diameter" (or smoothing length) of the kernel function with respect to particle i, $\boldsymbol{x}_{ij} = \boldsymbol{x}_i - \boldsymbol{x}_j$. n_1 and n_2 are taken as 6 and 4, respectively. $\overline{p}$ should be adjusted to suit the need of various problems.

Figure 1 is a flow chart of the approach. The solution begins with the import of geometry information. With geometry parameters, particles are generated, including the decision of particle initial positions, densities, strains and stresses. Once particles are generated, kernel functions and their derivatives can be determined. After all preparation work is done, the time advancement cycle begins by imposing loads and boundary constraints upon specific particles. Then, forces between different particles are computed using Eq. (7) – Eq. (9). Meanwhile, the anti-penetration force at the contact particles is also determined using Eq. (12). With all external and internal forces, velocities and displacements of the next time step are obtained using Eq. (10) and Eq. (11). The time advancement cycle repeats until the desired step number is reached.

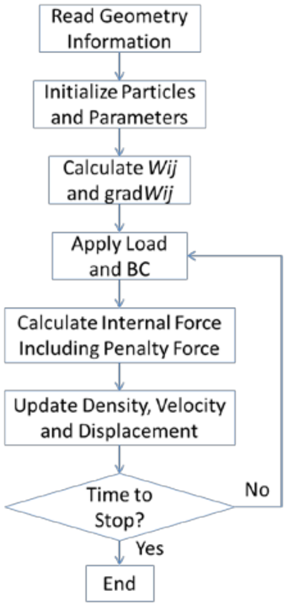

Fig. 1. Solution flow chart

STABILITY ANALYSIS SKETCH

One issue when applying SPH to solid problems is that instability occurs if part of the solid bears tensile stress, i.e., the so-called tension instability. Swegle et al. (1995) studied the stability of 1-dimension solid problem, and revealed that a sufficient condition for instability was $\frac{\mathrm{d}^2W}{\mathrm{d}x^2}\cdot\sigma^{xx} > 0$. Stability analysis shows that neither artificial viscosity nor time integration scheme is the main reason for tension instability. It is closely related to the smoothing kernel function.

Belytschko et al. (2000) found that using Lagrangian kernel based on the reference configuration can avoid tensile instability. Following this idea, the kernel function and its gradient in our approach are computed on the undeformed structure before time advancement. Once the kernel function and its gradient are predetermined, they keep unchanged during the entire simulation process. Using a typical Lagrange interpretation, this manner resembles the practice of FEM and FDM in preparing mesh only once before simulation. This practice not only improves the tolerance against tension instability, but also remarkably reduces computation cost. But it should be mentioned that small deformation is required in this treatment.

To investigate the stability behavior of the approach, we consider a simple rectangular computational domain, which is evenly divided into an a×b particle matrix as is illustrated in Fig.2. The x- and y-interval between two adjacent particles are identical, i.e., $\Delta x = \Delta y = \Delta$. We assume the smooth length of the kernel function is a small constant scalar (temporal and spatial independent) which makes one particle be influenced by only its four neighboring particles. Even though several assumptions are made to simplify the problem, the entire process of stability analysis is still lengthy. Hence, this section only gives a sketch of the analysis and detailed derivations are listed in Appendix A.

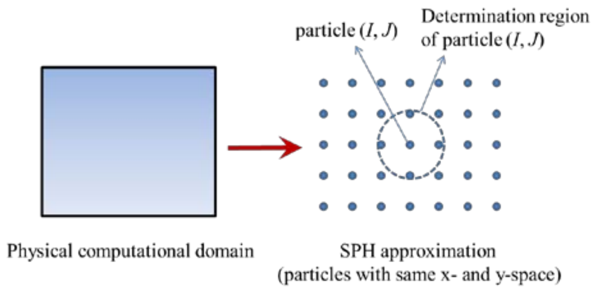

Fig. 2. Description of the planner problem to be used for stability analysis

Perturbation Propagation

Let the perturbations upon velocity and displacement have the form as $R_{I,J}^{n} \to R_{I,J}^{n} + \delta R_{I,J}^{n}$, $S_{I,J}^{n} \to S_{I,J}^{n} + \delta S_{I,J}^{n}$, $u_{I,J}{}^{n-1/2} \to u_{I,J}{}^{n-1/2} + \delta u_{I,J}{}^{n-1/2}$ and $v_{I,J}{}^{n-1/2} \to v_{I,J}{}^{n-1/2} + \delta v_{I,J}{}^{n-1/2}$, where subscripts I and J denotes the particle located at the I-th column and J-th row of the particle matrix in Fig. 2, which is also referred to as Particle (I, J) hereinafter. Here we use uppercase letters I, J to represent particle coordinates. By contrast lowercase letters i, j are employed to denote particle indexs. R and S are x- and y-component of displacement, u and v are x- and y-component of velocity. By adopting the basic formulas of SPH approach, one can write $\delta R_{I,J}^{n+1}$, $\delta S_{I,J}^{n+1}$, $\delta u_{I,J}{}^{n+1/2}$ and $\delta v_{I,J}{}^{n+1/2}$ in the expressions of $\delta R_{I,J}^{n}$, $\delta S_{I,J}^{n}$, $\delta u_{I,J}{}^{n-1/2}$ and $\delta v_{I,J}{}^{n-1/2}$. It should be mentioned that only linear terms are kept since nonlinearity leads to higher-order small quantity.

Fourier Expansion

Using Fourier expansion, the spatial distribution of the perturbation can be treated as the summation of components of various frequencies as

$$\left[\delta R(x,y)^{n}, \delta S(x,y)^{n}, \delta u(x,y)^{n-1/2}, \delta v(x,y)^{n-1/2}\right] = \sum_{m=1}^{M}\sum_{l=1}^{L}\left[R_{m,l}^{n}, S_{m,l}^{n}, u_{m,l}^{n-1/2}, v_{m,l}^{n-1/2}\right] e^{i(K_m x + Q_l y)}, \tag{13}$$

where $K_m = \dfrac{m\pi}{L_x}$, m=1, 2, 3, …, M, $M = L_x / \Delta x$, L_x is the x-directional extension of the computational domain, $Q_l = \dfrac{l\pi}{L_y}$, l=1, 2, 3, …, L, $L = L_y / \Delta y$, L_y is the y-directional extension of the computational domain. Using Eq. (13), the perturbation propagation equations can be reorganized as a series of sub-equations of various frequencies. The (m,l)-th sub-equation can be written as

$$\boldsymbol{e}_{m.l}{}^{n+1} = \mathbf{E}_{m,l}\boldsymbol{e}_{m.l}{}^{n}, \tag{14}$$

where $\boldsymbol{e}_{m.l}{}^{n} = \left[u_{m.l}{}^{n-1/2}, v_{m.l}{}^{n-1/2}, R_{m.l}{}^{n}, S_{m.l}{}^{n}\right]^{T}$. Eq. (14) only contains 4 unknowns and therefore is much simpler to solve.

Stability Analysis

If the approach is stable, i.e., the perturbation is not enlarged after a number of steps, it is required that the eigenvalues of $\mathbf{E}_{m,l}$ should not be larger than 1. Therefore, for each m and l, one stability requirement can be given. The final stability condition is obtained by combining all the M×L stability requirements. Under the assumption of Fig. 2, a sufficient condition for stability, after lengthy derivation, is written as

$$\Delta t \le \frac{\rho}{|mW'|}\sqrt{\frac{\rho(1-\mu)}{(3-\mu)G}} \quad \text{for plane stress problem,} \tag{15a}$$

$$\Delta t \le \frac{\rho}{|mW'|}\sqrt{\frac{\rho(1-2\mu)}{(3-4\mu)G}} \quad \text{for plane strain problem,} \tag{15b}$$

where m is the particle mass, $W' = \dfrac{\mathrm{d}}{\mathrm{d}r}W(r)\Big|_{r=\Delta}$.

The plane stress problem means $\sigma^{zz} = \sigma^{yz} = \sigma^{xz} = 0$, and plane strain problem $\varepsilon^{zz} = \varepsilon^{yz} = \varepsilon^{xz} = 0$. Eq. (15) reveals that the approach is conditionally stable.

VALIDATION AND APPLICATION

Here we verify the approach with two plane issues. The approach is then tested with a contact and collision problem.

Validation Case 1

In this case, one l×h rectangular plate is subject to triangular loads $\sigma_x = ky$ at its two opposite boundaries, as is shown in Fig. 3. The loads on the left and right boundary share the same magnitude but with opposite directions. In this case, we have l=h=5e-4m, k=50Pa/m, G=0.3Pa, E=0.39Pa and ρ=1000kg/m3. The plate is replaced with a 20×20 even-distributed particle matrix. Each particle represents a 2.5e-5m×2.5e-5m solid square, and the particle center coincides with the center of the solid square. Since a Gauss-type kernel function is used (i.e., $W(R,H)=\frac{1}{\pi H^2}e^{-(R/H)^2}$), the stability condition requires $\Delta t \le 0.0018$ s, and therefore we take $\Delta t = 0.0005$ s during simulation. One principle during the decision of particle distribution is that the adjacent particle distance is preferred to be identical in both directions if possible. Or at least the difference between adjacent particle distance in two directions should be not too big. The total particle amount should be enough to get the required precision, but needs not to be too large as computational cost may be improved greatly.

Fig. 4 depicts particle distribution of the deformed plate predicted by the SPH approach, with and without conducting the kernel function normalization. In the left subplot (no normalization), one can observe an evident distinction between the SPH and theoretical results at the two bottom corners, since the SPH integral losses 3/4 of its integral region at corners. Yet the two results seem to show well agreement at the rest part of the plate. However, by normalization, the error induced by integral region truncation is effectively eliminated in the right subplot. Fig. 5 displays strain tensor components ε_x and ε_y in a vector form [ε_x , ε_y], and indicates that SPH gives good approximation on strains. Fig. 6 compares the logarithm of vonMises stress predicted by various methods. Fig. 7 shows the distribution of vonMises stress along the left edge of the plate, which points out that normalization of the SPH kernel function is essential to obtain reliable results.

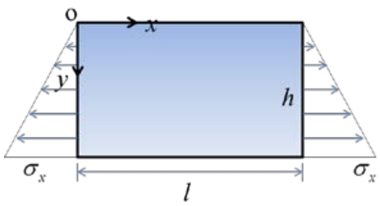

Fig. 3. Problem description of validation case 1

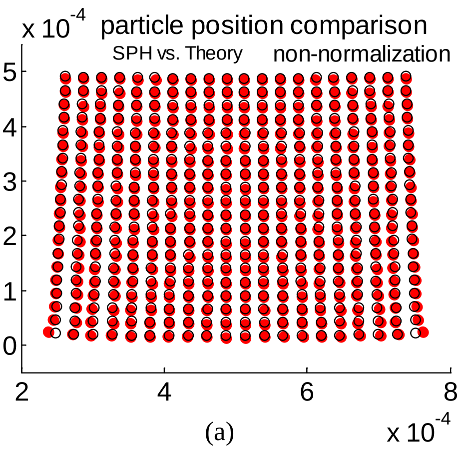

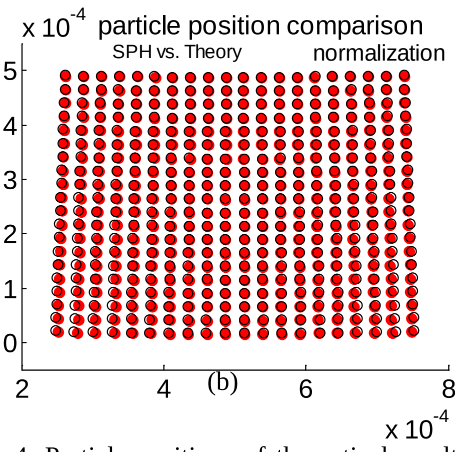

Fig. 4. Particle positions of theoretical results (dark unfilled circle) and SPH results (red filled circle), with (a) and without (b) kernel function normalization

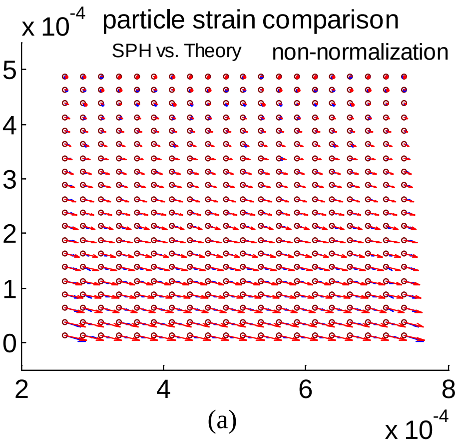

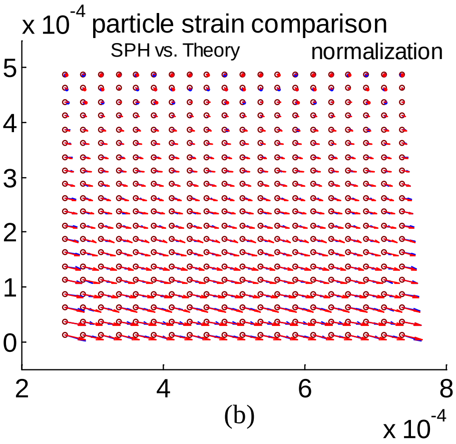

Fig. 5. Strain vectors [ε_x , ε_y] of theoretical results (red arrows) and SPH results (blue arrows), with (a) and without (b) kernel function normalization

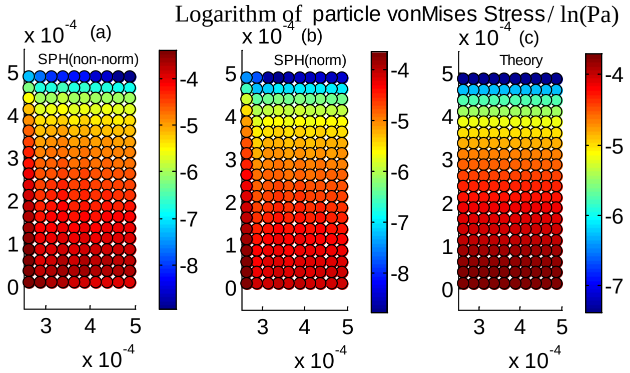

Fig. 6. Logarithm of particle vonMises stress of half plate, with (a) SPH results without normalization, (b) SPH results with normalization, and (c) theoretical results

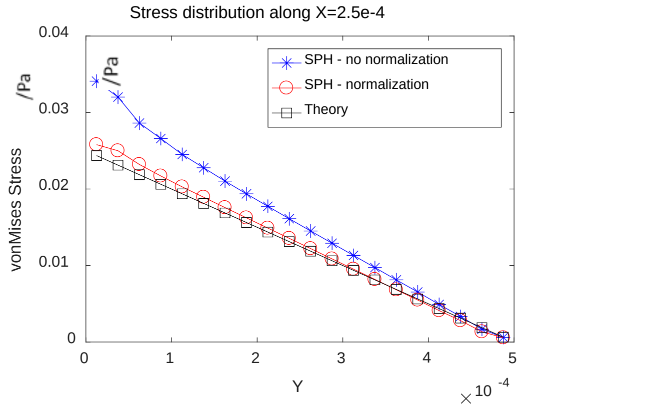

Fig. 7. Distribution of vonMises stress along the left edge of the plate (x=2.5e-4)

Validation Case 2

This example studies the deformation of an annulus plate under shear stress. As is shown in Fig. 8, the inner and outer radiuses of the annulus are a and b, respectively. The shear stresses upon inner and outer boundary are $\tau_1 = -q/a^2$ and $\tau_2 = q/b^2$, respectively. In this case, we have a=2.5e-4m, b=5e-4m, q=1.7227e-9N, G=0.3Pa, E=0.39Pa and ρ=1000kg/m3. The annulus plate is uniformly divided into 36 particles along the circumferential direction, and 10 particles along the radial direction. This case also adopts Gauss-type kernel function and requires a stability condition of $\Delta t \le 0.0018$ s. During simulation Δt is taken as 0.0005s.

Fig. 9 compares SPH and theoretical results in particle displacement. Since no corner exists in this problem, the solver gives acceptable results even though no normalization is used. With a well-selected smoothing length, the precision reduction on domain boundary may be caused by the loss of only one particle. The vonMises stresses computed with various methods are shown in Fig. 10. In Fig. 10, subplot (b) (SPH results with normalization) shows better approximation of the theoretical results. Fig. 11 displays the distribution of vonMises stress along the radial direction of the ring plate. As can be seen in Fig. 11, by performing kernel function normalization, the stress disagreement against theoretical results can be reduced.

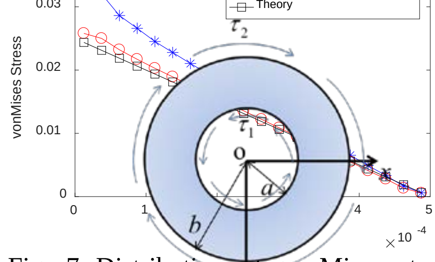

Fig. 7 Distribution of vonMises stress along the left edge of the plate (x=2.5e-4)

Fig. 8. Problem description of validation case 2

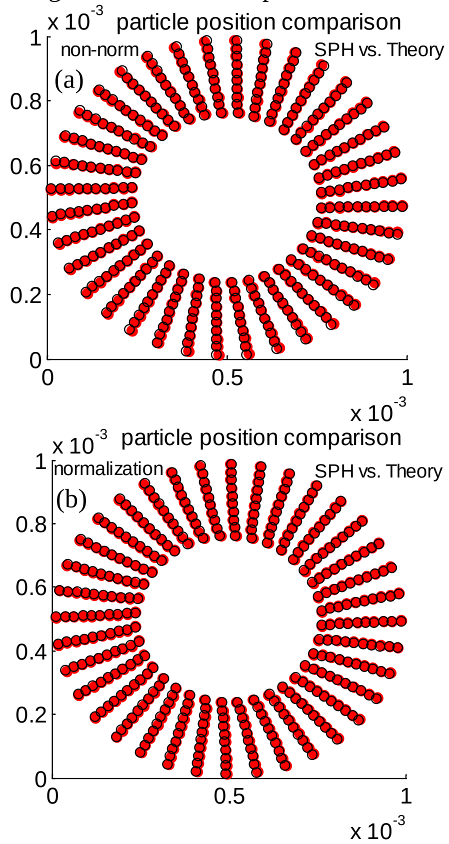

Fig. 9. Particle positions of theoretical results (dark unfilled circle) and SPH results (red filled circle), with (a) and without (b) kernel function normalization

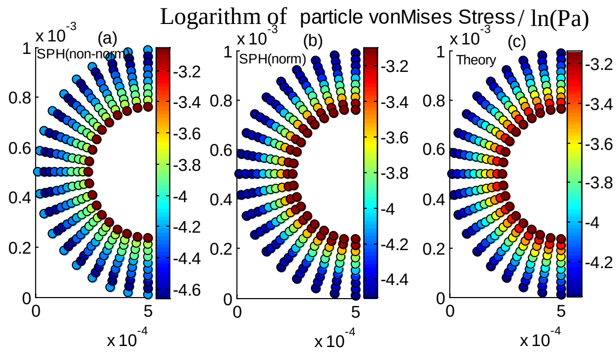

Fig. 10. Logarithm of particle vonMises stress of half plate, with (a) SPH results without

normalization, (b) SPH results with normalization, and (c) theoretical results

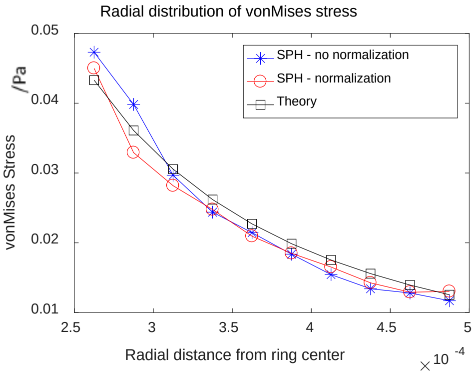

Fig. 11. Radial distribution of vonMises stress within the ring plate

Stability tests

In this subsection, the square plate of validation case 1 is adopted, but with a series of triangle stresses. Let the triangle stress of validation case 1 be denoted as T. The loads of various tests, which are numbered from (a) to (g), are listed in Table 1. Since stability condition requires $\Delta t \leq 0.0018$ s, we take $\Delta t = 0.0005$ s for all the cases.

Fig. 12 and Fig. 13 depict SPH particle locations and vonMises stress distributions (color map) when stable statuses are reached, calculated without and with kernel function normalization, respectively. The degree of particle dispersion increases noticeably with the growth of the tensile force. In subplot (g), huge particle separation can be observed in the vicinity of the plate corner. Nevertheless, the approach can give stable solutions even at large deformation (namely at large tensile force). Besides, kernel function normalization does not affect the approach's tolerance against tension instability. Once the time step is small enough, the instability phenomenon will not happen with or without kernel function normalization. However, the kernel function normalization affects the solution precision which is the main reason for the difference between Fig. 11 and Fig. 12.

Fig. 14 shows maximum displacement and stress of each load case and a strict linear regularity can be concluded. Noticing that the PDEs to be solved are linear, the approach successfully preserves the property of the governing PDEs. In methods such as FEM and FDM, the linearity can also be preserved due to the resulted linear matrix system. However, linearity can be wrecked in a traditional SPH method.

/Pa

Table 1 Loads of various tests

Case	Load	Case	Load	Case	Load	Case	Load
(a)	T	(b)	$2T$	(c)	$4T$	(d)	$8T$
(e)	$16T$	(f)	$32T$	(g)	$64T$		

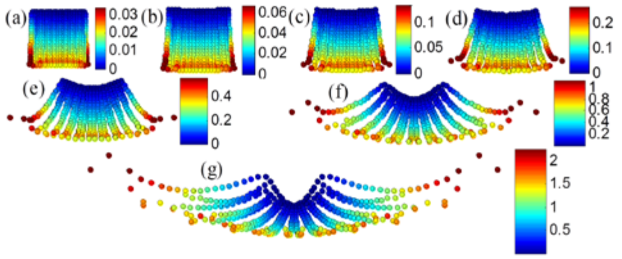

Fig. 12. SPH Particle distributions (without normalization) of the square plate subject to various load cases

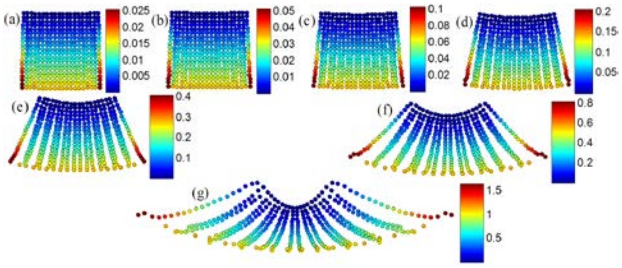

Fig. 13. SPH Particle distributions (with normalization) of the square plate subject to various load cases

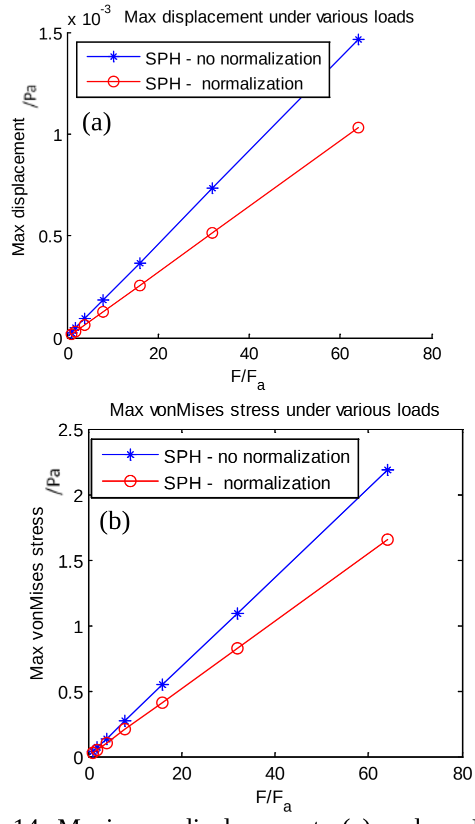

Fig. 14. Maximum displacements (a) and vonMises stresses (b) of the square plate under various loads Fs, where Fa denotes the load of case (a)

Fig. 15. displays the critical time steps of various test cases. A critical time step, denoted as Δt_c, is defined such that the solution is stable for $\Delta t \leq \Delta t_c$ and unstable for $\Delta t > \Delta t_c$. The critical

time steps are determined by solving the problem repeatedly with various time steps and finding the time step when the solution turns right from unstable to stable. It can be seen that Δt_c is not affected by external tension loads, indicating that no tension instability happens. Yet kernel function normalization does affect stability behavior. Fig. 16 shows critical time steps under various smoothing lengths of the kernel function. In Fig. 16, a minimum critical time step exists both with and without kernel function normalization. The kernel function normalization activity improves stability when the smoothing length is small, yet harms stability when the smoothing length becomes large. Fig. 17 shows that the critical time step increases with the growth of density, or with the reduction of shear modulus. Moreover, it demonstrates that Eq. (15) is sufficient to ensure the stability of solution.

Fig. 18 gives a typical exhibition on how particles move when the simulation time step exceeds Δt_c. It can be observed that the instability starts from the bottom corners where the maximum force is imposed. Soon the inner particles are influenced and begin to escape from their original locations. The unstable motion of one particle can extend to its neighboring particles, making instability grow exponentially. Finally, when all particles become unstable, an 'explosion' is induced and the solution fails, which is a typical CFL instability phenomenon.

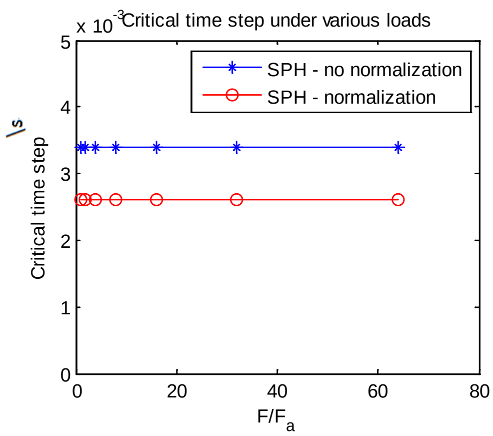

Fig. 15. Critical time steps under various loads, where Fa denotes the load of case (a)

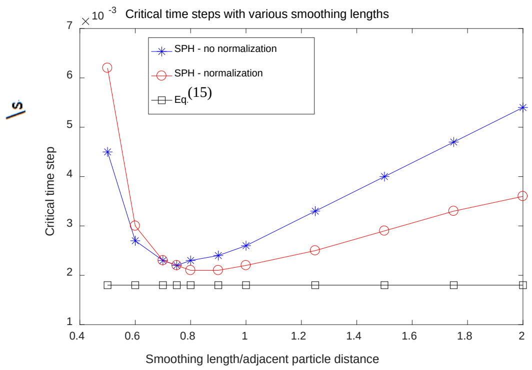

Fig. 16. Critical time steps changing with various smoothing lengths of the kernel function

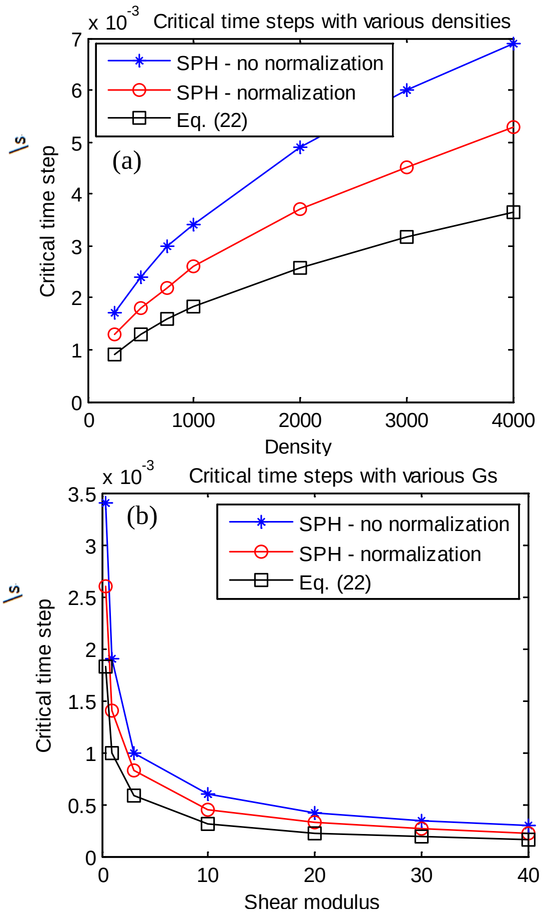

Fig. 17. Critical time steps changing with various densities (a) and shear modulus (b)

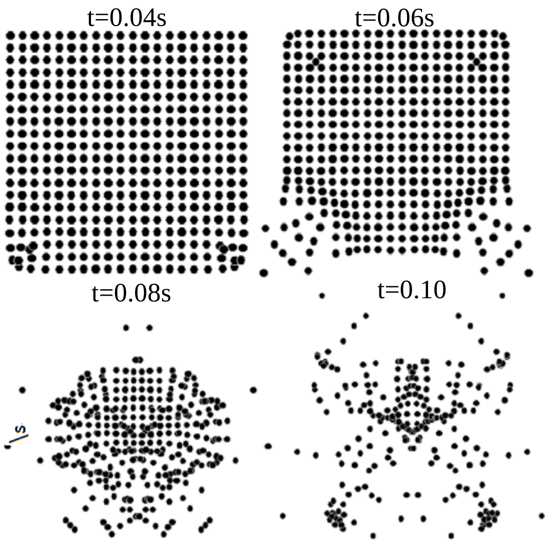

Fig. 18. Typical evolution of particle distribution when instability occurs ($\Delta t = 0.004$ s)

Application

This subsection tests the proposed approach with a contact and collision issue. As is shown in Fig.

19, an annulus plate, a rectangular plate and a horizontal rigid solid wall are sited at different heights. When simulation begins, the annulus and rectangular plate start to drop down under gravity. Once the rectangular plate meets the solid wall, it gets rebounded and collides with the annulus plate. In this instance, the inner and outer radius of the annulus are a=2.5e-4m and b=5e-4m, respectively. The width and height of the rectangle are l=5e-4m and h=2.5e-4m. The initial positions are z1=-1e-4m, z2=1.35e-4m and z3=1.26e-3m. Gravitational acceleration is g=-9.8m/s2, Young's modulus is E=650Pa, and the density of the annulus and rectangle are ρ=1000kg/m3. Two particles, which are numbered as 14 and 183 and will be studied later, are shown in Fig. 19. The annulus and rectangle are discretized with 36×5 (circumferential×radial) and 20 × 10 (horizontal × vertical) particles, respectively. Kernel function normalization is conducted. The stability condition requires that $\Delta t \leq 0.0001$ s and we therefore take $\Delta t = 0.00002$ s.

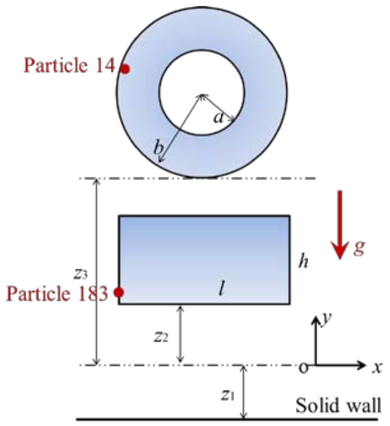

Fig. 19. Description of the contact and collision problem

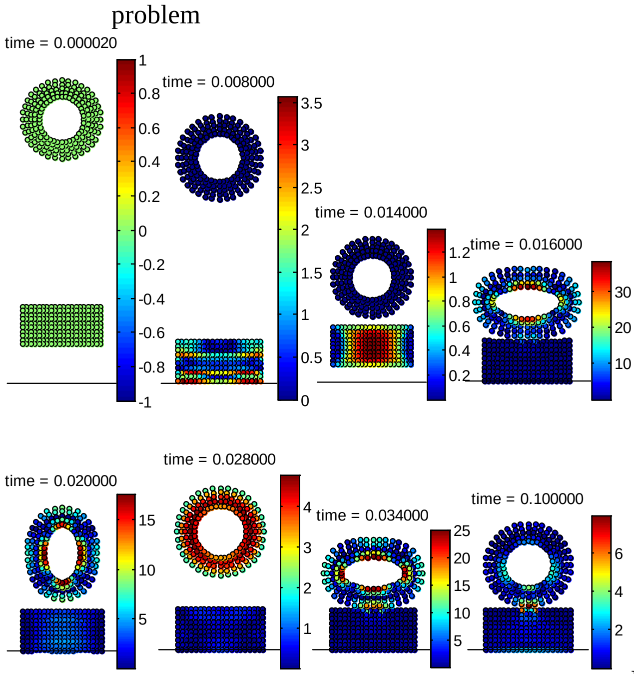

Fig. 20. Snapshots of the collision of an annulus and a rectangular object (vonMises stresses in colored maps)

Fig. 20 gives snapshots of various moments, with particles filled with different colors according to the local vonMises stress. During collision, the annulus experiences large deformation and vibration together with translational rigid-body movement. On the contrary, the deformation and vibration of the rectangle are inconspicuous. The maximum vonMises stress occurs when the annulus meets the rectangle for the first time. Fig. 21 analyzes the displacement histories of particle 14 and 183. In y-directional displacement, evident regular reciprocation which represents rigid-body movement can be observed. The localized vibration can be clearly revealed in the x-directional plot.

To obtain the natural frequencies of the two objects, Fig. 22 performs Fourier transformation upon x-displacement histories. It is worth noting that time histories between t=0.033s and t=0.1s are not included in Fourier transformation, for the purpose of eliminating the influence of solid-body movement. Fig. 22 reveals that a number of modes are stimulated during collision, yet only the first 3 frequencies are concerned here. Table 2 lists the first 3 natural frequencies predicted by both SPH and FEM, which show a good agreement with each other.

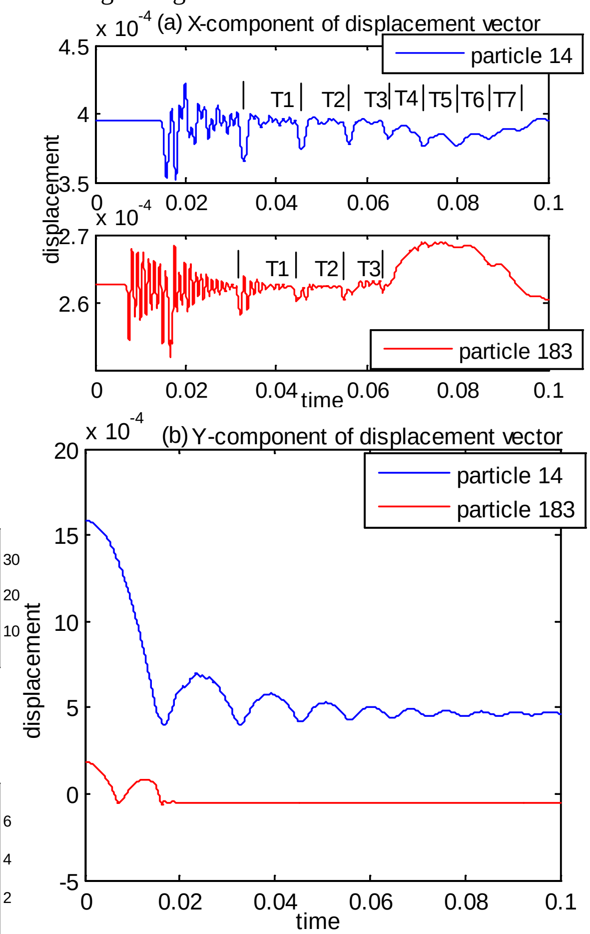

Fig. 21. Displacement histories (in meters) of particle

14 and particle 183, with (a) x component and (b) y component

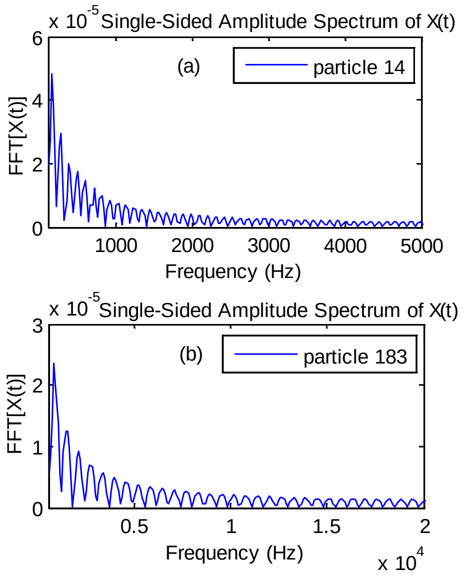

Fig. 22. Fast Fourier transform on the x-directional displacement histories of (a) particle 14 and (b) particle 183

Table 2 Natural frequencies of the annulus and rectangular plate calculated by SPH and FEM

Frequency No.	Annulus frequencies			Square frequencies		
	SPH (Hz)	FEM (Hz)	error	SPH (Hz)	FEM (Hz)	error
1	146.5	152.5	4.0%	878.9	874.3	0.5%
2	366.2	356.0	2.9%	1465	1415	3.5%
3	468.3	445.3	5.2%	2148	2058	4.4%

CONCLUSIONS

This paper adopts SPH method to solve elastic solid problems. Using a Lagrange idea, kernel function and its derivative are determined only once at the beginning of simulation. By adopting special treatment at the contact surface, the approach is applicable to dynamic contact issues. The main conclusions of the paper are as follows.

1. The approach gives reasonable and reliable solution on dynamic and static elastic solid problems, and hence can be an alternative to the traditional Finite Element Method.

2. By predetermining the kernel function and its derivative, the approach lowers computation cost and exhibits good tolerance against tension instability. By performing a von Neumann stability analysis, it is proved that tension instability can be completely avoided under certain condition.

3. Being a sufficient condition of stability, Eq. (15) can be used to ensure stability.

4. Kernel function normalization is necessary to ensure the accuracy of the approach, especially when the solution domain contains sharp corners.

ACKNOWLEDGMENT

This research was financed by the State Key Program of National Natural Science of China (grant No. 51439004), the National Natural Science Foundation of China (Grant No. 51609101 and 51909103), the Natural Science Foundation of Fujian Province of China (Grant No. 2017J01701 and 2017J05085), and the Outstanding Young University Scientific Research Talents Cultivation Plan of Fujian Province of China.

REFERENCES

Antoci, C., Gallati, M., Sibilla, S., 2007. Numerical simulation of fluid–structure interaction by SPH. Computers & Structures, 85(11), 879-890.

Belytschko, T., Guo, Y., Liu, W. K., 2000. A unified stability analysis of meshless particle methods. International Journal for Numerical Methods in Engineering 48(9): 1359-1400.

Bouscasse, B., Colagrossi, A., Marrone, S., Souto-Iglesias, A., 2017. SPH modelling of viscous flow past a circular cylinder interacting with a free surface. Computers & Fluids, 146, 190-212.

Chen, J. K., Beraun, J. E., Jih, C. J., 1999. An improvement for tensile instability in smoothed particle hydrodynamics. Computational Mechanics, 23(4), 279-287.

Chikazawa, Y., Koshizuka, S., Oka, Y., 2001. A particle method for elastic and visco-plastic structures and fluid-structure interactions. Computational Mechanics, 27(2), 97-106.

Dyka, C. T., Ingel, R. P., 1995. An approach for tension instability in smoothed particle hydrodynamics (SPH). Computers & structures, 57(4), 573-580.

Gómez-Gesteira, M., Crespo, A. J., Rogers, B. D., Dalrymple, R. A., Dominguez, J. M., Barreiro, A., 2012. SPHysics–development of a free-surface fluid solver–Part 2: Efficiency and test cases. Computers & Geosciences, 48, 300-307.

Gray, J. P., Monaghan, J. J., Swift, R. P., 2001. SPH elastic dynamics. Computer Methods in Applied Mechanics and Engineering, 190(49-50), 6641-6662.

Hu, X. Y., Adams, N. A., 2015. A SPH model for incompressible turbulence. Procedia IUTAM, 18, 66-75.

Lin, J., Naceur, H., Coutellier, D., Laksimi, A., 2014. Geometrically nonlinear analysis of thin-walled structures using efficient Shell-based SPH method. Computational Materials Science, 85, 127-133.

Liu, M. B., Liu, G. R., 2010. Smoothed particle hydrodynamics (SPH): an overview and recent developments. Archives of computational methods in engineering, 17(1), 25-76.

Monaghan, J. J., 1994. Simulating free surface flows with SPH. Journal of computational physics, 110(2), 399-406.

Monaghan, J. J., 2000. SPH without a Tensile Instability. Journal of Computational Physics, 159(2), 290-311.

Peng, C., Xu, G., Wu, W., Yu, H. S., Wang, C., 2017. Multiphase SPH modeling of free surface flow in porous media with variable porosity. Computers and Geotechnics, 81, 239-248.

Ren, B., Wen, H., Dong, P., Wang, Y., 2016. Improved SPH simulation of wave motions and turbulent flows through porous media. Coastal Engineering, 107, 14-27.

Sarfaraz, M., Pak, A., 2017. SPH numerical simulation of tsunami wave forces impinged on bridge superstructures. Coastal Engineering, 121, 145-157.

Sigalotti, Leonardo D. G., Lopez, H., 2008. Adaptive kernel estimation and SPH tensile instability. Computers and Mathematics with Applications, 55(1), 23-50.

Sugiura, K., Inutsuka, S. I., 2017. An extension of Godunov SPH II: Application to elastic dynamics. Journal of Computational Physics, 333, 78-103.

Swegle, J. W., Hicks, D. L., Attaway, S. W., 1995. Smoothed particle hydrodynamics stability analysis. Journal of computational physics, 116(1), 123-134.

Xu, X., Deng, X. L., 2016. An improved weakly compressible SPH method for simulating free surface flows of viscous and viscoelastic fluids. Computer Physics Communications, 201, 43-62.

Zhang, C., Hu, X. Y., Adams, N. A., 2017. A weakly compressible SPH method based on a low-dissipation Riemann solver. Journal of Computational Physics, 335, 605-620.

APPENDIX

A. Stability analysis

A.1 Perturbation propagation equations

The perturbation propagation of velocity is

$$\delta u_{I,J}{}^{n+1/2} = \delta u_{I,J}{}^{n-1/2} + \frac{\Delta t\left(mW'\right)^2}{\rho^3}\left[\begin{array}{l}\gamma\left(\begin{array}{l}\delta R^n_{I-2,J} + \delta R^n_{I+2,J} - 2\delta R^n_{I,J} + \\ \delta S^n_{I-1,J-1} - \delta S^n_{I-1,J+1} - \delta S^n_{I+1,J-1} + \delta S^n_{I+1,J+1}\end{array}\right) + \\ \frac{G}{2}\left(\begin{array}{l}2\delta R^n_{I-2,J} - 6\delta R^n_{I,J} + 2\delta R^n_{I+2,J} + \delta R^n_{I,J+2} + \delta R^n_{I,J-2} \\ -\delta S^n_{I-1,J+1} + \delta S^n_{I+1,J+1} + \delta S^n_{I-1,J-1} - \delta S^n_{I+1,J-1}\end{array}\right)\end{array}\right], \quad (A.1)$$

$$\delta v_{I,J}{}^{n+1/2} = \delta v_{I,J}{}^{n-1/2} + \frac{\Delta t\left(mW'\right)^2}{\rho^3}\left[\begin{array}{l}\gamma\left(\begin{array}{l}\delta R^n_{I-1,J-1} - \delta R^n_{I+1,J-1} - \delta R^n_{I-1,J+1} + \delta R^n_{I+1,J+1} \\ +\delta S^n_{I,J-2} - 2\delta S^n_{I,J} + \delta S^n_{I,J+2}\end{array}\right) + \\ \frac{G}{2}\left(\begin{array}{l}\delta R^n_{I-1,J-1} - \delta R^n_{I-1,J+1} - \delta R^n_{I+1,J-1} + \delta R^n_{I+1,J+1} + \\ 2\delta S^n_{I,J-2} - 6\delta S^n_{I,J} + 2\delta S^n_{I,J+2} + \delta S^n_{I-2,J} + \delta S^n_{I+2,J}\end{array}\right)\end{array}\right]. \quad (A.2)$$

The perturbation propagation of displacement is

$$\delta R^{n+1}_{I,J} = \delta R^n_{I,J} + \Delta t \cdot \delta u_{I,J}{}^{n+1/2}, \quad (A.3)$$

$$\delta S^{n+1}_{I,J} = \delta S^n_{I,J} + \Delta t \cdot \delta v_{I,J}{}^{n+1/2}, \quad (A.4)$$

where superscript n denotes values at the n-th time step, m is particle mass, G is shear modulus, γ is $\frac{\mu}{1-2\mu}G$ for plane strain problem and $\frac{\mu}{1-\mu}G$ for plane stress problem, μ is Poisson ratio, and $W' = W'\left(\Delta\right)$.

A.2 Fourier expansion

The error evolution matrix of Eq. (14) is

$$\mathbf{E}_{m,l} = \begin{bmatrix} 1 & 0 & \Delta t A_{m,l} & \Delta t B_{m,l} \\ 0 & 1 & \Delta t B_{m,l} & \Delta t A_{m,l} \\ \Delta t & 0 & 1+\Delta t^2 A_{m,l} & \Delta t^2 B_{m,l} \\ 0 & \Delta t & \Delta t^2 B_{m,l} & 1+\Delta t^2 A_{m,l} \end{bmatrix}, \quad (A.5)$$

where

$$A_{m,l} = \frac{\left(mW'\right)^2}{\rho^3}\left[2\left(\gamma+G\right)\cos 2K_m\Delta + G\cos 2Q_l\Delta - 2\gamma - 3G\right], \quad (A.6)$$

$$B_{m,l} = \frac{\left(mW'\right)^2}{\rho^3}\left(2\gamma+G\right)\left[\cos\left(K_m+Q_l\right)\Delta - \cos\left(K_m-Q_l\right)\Delta\right]. \quad (A.7)$$

A.3 Stability analysis

The eigenvalues of $\mathbf{E}_{m,l}$ are

$$\lambda_{1,2,3,4} = \frac{t^2}{4}\left(\pm P + A + C\right) \pm \frac{2^{1/4}}{4}\left[\begin{array}{l}\left(A^2+2B^2+C^2+AP+CP\right)t^4 \\ +4\left(A+C+P\right)t^2\end{array}\right]^{1/2} + 1, \quad (A.8)$$

where A, B, C and t are short for $A_{K,Q}$, $B_{K.Q}$, $A_{Q,K}$, and Δt, respectively, and $P = \left(A^2 - 2AC + C^2 + 4B^2\right)^{1/2}$. Stability condition indicates that $\left|\lambda_{1\,(and\ 2,3,4)}\right|^2 \le 1$, thereby requiring

$$t^2 \le \frac{2}{\sin^2 K_m\Delta + \sin^2 Q_l\Delta} \cdot \min\left(\frac{1}{cG}, \frac{1}{2c(\gamma+G)}, \frac{1}{c(2\gamma+3G)}\right). \quad (A.9)$$

where $c = (mW')^2 / \rho^3$. Eq. (A.9) holds for all $K_m\Delta = m\pi / M \in (0, \pi)$ and $Q_l\Delta = l\pi / L \in (0, \pi)$, namely

$$t^2 \le \frac{1}{c(2\gamma+3G)}. \quad (A.10)$$

Using the expression of c and γ, stability condition Eq.(15) can be obtained.

B. Analytical solution of validation case 1 & 2

The analytical solution of validation case 1 is given by

$$\begin{cases} \sigma_x = ky, \quad \sigma_y = 0, \quad \tau_{xy} = 0 \\ \varepsilon_x = ky / E, \quad \varepsilon_y = -\mu ky / E, \quad \gamma_{xy} = 0 \\ s_x = \dfrac{k}{E}(x - l/2)y, \quad s_y = \dfrac{k}{2E}\left[-\mu y^2 - (x - l/2)^2\right] \end{cases}, \quad (B.1)$$

where s_x and s_y are x and y directional deformation, ε_x, ε_y and γ_{xy} are x, y directional normal strain and shear strain respectively, σ_x, σ_y and τ_{xy} are x, y directional normal stress and shear stress respectively. E is Young's modulus, μ is Poisson ratio, and k is the control parameter of the triangle load.

The analytical solution of validation case 2 is given by

$$\begin{cases} \sigma_r = \sigma_\theta = 0, \ \tau_{\theta r} = q / r^2 \\ \varepsilon_r = \varepsilon_\theta = 0, \ \gamma_{\theta r} = \dfrac{2(1+\mu)}{E}\dfrac{q}{r^2} \\ s_r = 0, \quad s_\theta = -\dfrac{1+\mu}{E}\dfrac{q}{r} \end{cases}, \quad (B.2)$$

where s_r and s_θ are radial and circumferential deformation, ε_r, ε_θ and $\gamma_{\theta r}$ are radial, circumferential strain and shear strain respectively, σ_r, σ_θ and $\tau_{r\theta}$ are radial, circumferential stress and shear stress respectively.